Offshore platform sourced pollution monitoring using space-borne fully polarimetric C and X band synthetic aperture radar

Suman Singha *, Rudolf Ressel

Maritime Safety and Security Lab, Remote Sensing Technology Institute (IMF), German Aerospace Center (DLR), Henrich Focke Str. 4, 28199 Bremen, Germany

ARTICLE INFO

ABSTRACT

Use of polarimetric SAR data for offshore pollution monitoring is relatively new and shows great potential for operational offshore platform monitoring. This paper describes the development of an automated oil spill detection chain for operational purposes based on C-band (RADARSAT-2) and X-band (TerraSAR-X) fully polarimetric images, wherein we use polarimetric features to characterize oil spills and look-alikes. Numbers of near coincident TerraSAR-X and RADARSAT-2 images have been acquired over offshore platforms. Ten polarimetric feature parameters were extracted from different types of oil and 'look-alike' spots and divided into training and validation dataset. Extracted features were then used to develop a pixel based Artificial Neural Network classifier. Mutual information contents among extracted features were assessed and feature parameters were ranked according to their ability to discriminate between oil spill and look-alike spots. Polarimetric features such as *Scattering Diversity*, *Surface Scattering Fraction* and *Span* proved to be most suitable for operational services.

© 2016 Elsevier Ltd. All rights reserved.

1. Introduction

Operational detection and discrimination of oil spills over oceans have received considerable attention due to their impact on marine ecosystem from an environmental and political point of view. Space-borne Synthetic Aperture Radar (SAR) has been proven to be indispensable for operational offshore pollution monitoring and attracting significant research interest (Fingas and Brown, 2014; Singha et al., 2013, 2014; Solberg, 2012; Topouzelis, 2008; Brekke and Solberg, 2005). One major focus regarding oil spill monitoring concentrates on offshore platforms, where operational discharge occurs regularly. As most of the offshore platforms reside in environmentally sensitive zones and also near to coastal regions (e.g. North Sea and Bombay High platforms clusters), it poses a major long-term threat to marine and coastal ecosystems (Carpenter, 2016; Singha et al., 2014). Until now, most of the operational and Near Real Time (NRT) oil spill detection techniques use single-polarization (mainly VV polarization and ground range projected) intensity SAR images where oil spills appear as dark-spots. The sea surface roughness responsible for SAR backscatter is primarily produced by capillary and small gravity waves generated by local winds. Damping of these waves by oil slicks reduces the backscatter, resulting in dark areas in SAR images. Although spaceborne SAR systems have proven to be a valuable tool for oil spill detection and monitoring, the major challenge still remains, i.e. discrimination between oil spill and 'look-alike' spots (Zhang et al., 2011; Solberg, 2012). In the last decade, a number of

automatic and semi-automatic techniques have been implemented in order to differentiate oil spill and look-alike dark spots based on single-pol (HH or VV, multi-looked ground range projected) SAR images. Some of the proposed techniques are also capable of providing results in Near Real Time (NRT) (Singha et al., 2014). However, such techniques suffer from a high miss-classification rate which is undesirable for operational services. Recently improved availability of polarimetric SAR data makes it attractive to utilize such data in a time critical processing chain capable of detecting and distinguishing different types of oil spills from 'look-alikes'. In addition to that, small operational spillages (production water) from offshore platforms are often ignored as their manifestations appear insignificant on traditional 'ScanSAR' wide swath images which can be overcome with high resolution polarimetric imagery. Therefore, in order to utilize those advantages a major focus of research in this area is the development of automated algorithms based on polarimetric images to distinguish oil spills from 'look-alikes'. This study investigates, for the first time, spatially and temporally coincident, fully polarimetric C and X band spaceborne SAR images in order to develop an oil spill detection methodology. Traditional oil spill detection techniques use backscatter, geometry, shape, or contextual based feature parameters in order to classify dark-spots on object basis, whereas this study aims to develop a pixel based classifier to distinguish oil spill and 'look-alike' spots and eventually different types of oil. A comprehensive review of traditional oil spill detection methodologies and evaluation of traditional features can be found in Topouzelis (2008) and Singha et al. (2014), respectively. On the other hand, numerous polarimetric features have been proposed for the same purpose (Migliaccio et al., 2007, 2009b; Velotto et al., 2011; Skrunes et al., 2014a, 2014b; Migliaccio et al.,

* Corresponding author.
E-mail addresses: Suman.Singha@dlr.de (S. Singha), Rudolf.Ressel@dlr.de (R. Ressel).
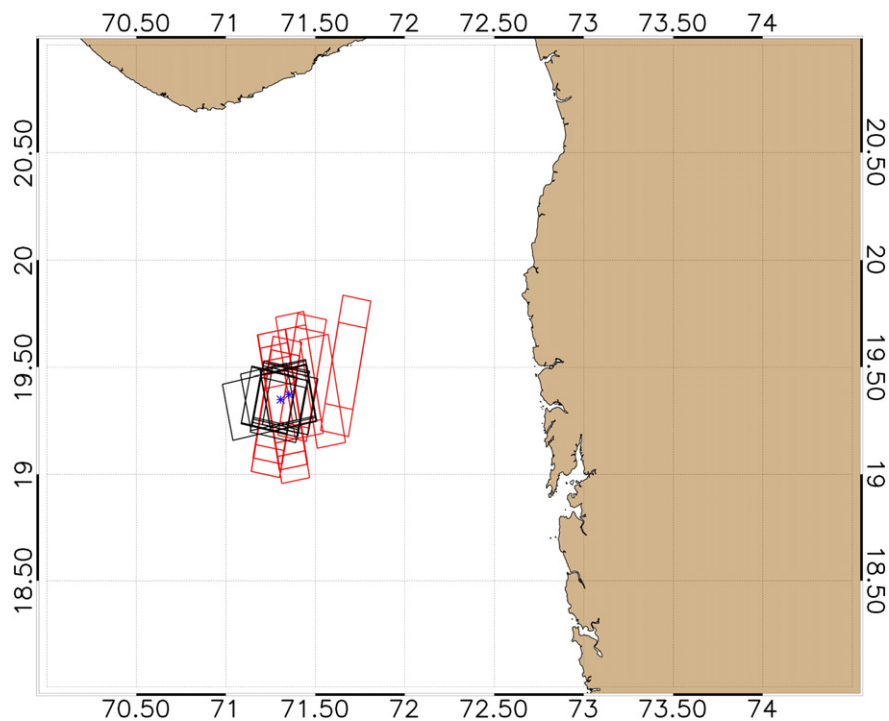
Fig. 1. Footprints of TerraSAR-X QuadPol StripMap (shown in red rectangles) and RADARSAT-2 Fine QuadPol (shown in black rectangles) images acquired over Bombay High offshore platform cluster (approximate location of platform clusters shown in blue marks).

2009a; Nunziata et al., 2011; Minchew, 2012; Liu et al., 2011; Zhang et al., 2011; Collins et al., 2015). This study focuses on developing an Artificial Neural Network (ANN) based classifier which uses ten different polarimetric features to distinguish oil spills from 'look-alikes'. In addition to that, this study also looks into the performance of different polarimetric features for their ability to discriminate between different types of oil and 'look-alikes' in the fully polarimetric C and X band domain.

SAR sensors with fully polarimetric capabilities are now available in L (ALOS-2 PALSAR), C (RADARSAT-2, RISAT) and X (TerraSAR-X; Experimental Mode) band and proven to be suitable for oil spill detection. Forthcoming SAR sensors like RADARSAT Constellation Mission (RCM) with Compact Polarimetry and larger swath coverage, NISAR with Multi Frequency (S and L band) fully Polarimetric sensors will certainly influence the SAR based oil spill detection paradigm in near future. Methodologies for oil spill detection systems based on multi-mission polarimetric SAR sensors have been continuously evolving and development of an operational NRT processing chain is highly desirable (Solberg, 2012; Singha et al., 2016). While previously developed methodologies based on single polarimetric images manage to produce reasonable classification accuracy required for operational services, in most of the cases they suffer from a significant false positive rate and still require a manual interaction Singha et al. (2014). This warrants an investigation into the polarimetric domain. Recent investigations show unique benefits of polarimetric SAR data to both observe oil slicks and discriminate between oil spill and look-alike spots which is still a major challenge for traditional oil spill detection systems based on single polarized SAR images (Migliaccio et al., 2007; Singha et al., 2016). The polarimetric scattering characteristics of the oil-covered sea surface depends on a host of contributing parameters such as Substance type (e.g. volume, age, and viscosity of the spilled oil), SAR instrument specific parameters (e.g. incidence angle, noise floor, imaging mechanism), Geophysical parameters (e.g. local wind vector, presence of capillary waves, surface currents). Moreover, even the molecular structure and emulsification processes of the oil can affect the dielectric properties of oil-covered waters and their scattering properties.

In this present study we developed an automated oil spill detection methodology using Artificial Neural Network (ANN) as a classifier which was trained using ten different polarimetric features extracted from C (RADARSAT-2) and X band (TerraSAR-X, Dual Receave Antenna Mode) fully polarimetric SAR images. The classifier is designed to classify each image into four different classes i.e. Crude Oil (CO), Emulsion (EM), Look-Alike (LA) and Open Water (OW). Alongside fully polarimetric C band SAR images this study also examines for the first time the potential of X-band fully polarimetric space borne SAR acquisitions for oil spill detection and characterization. The paper is organized as follows: Section 2 provides the description of the dataset used in this study. Section 3 gives an introduction about the polarimetric features and their mathematical definitions. Section 4 provides the summary of the proposed methodology and the processing chain along with a comprehensive scheme to analyze the discriminative power of polarimetric and traditional features. Experimental results and discussions about the performance of the classifier and feature analysis are presented in Section 5, while summary and conclusions are drawn in Section 6.

2. Experimental dataset

Fully polarimetric TerraSAR-X (TS-X) and RADARSAT-2 (RS-2) images have been used to develop and validate the proposed algorithm. The majority of the images were acquired over the Bombay High region, about 160 km off the coast of Mumbai, India. This region hosts a cluster of offshore oil platforms and has been in production since 1974. Unlike European waters, there are no observation derived from regular aerial surveillance, wherefore the only possible way to monitor this kind of area is the use satellite SAR imagery. Beginning from March 2015 until the October 2015, a total number of 20 TerraSAR-X images and 20 RADARSAT-2 images were acquired over the study area. Efforts have been made to ensure that the C and X-band acquisitions are spatially and temporally near coincident. In addition to the dataset collected over Bombay High region we have also gathered a number of TS-X and RS-2 fully polarimetric images manifesting 'look-alike' spots. The
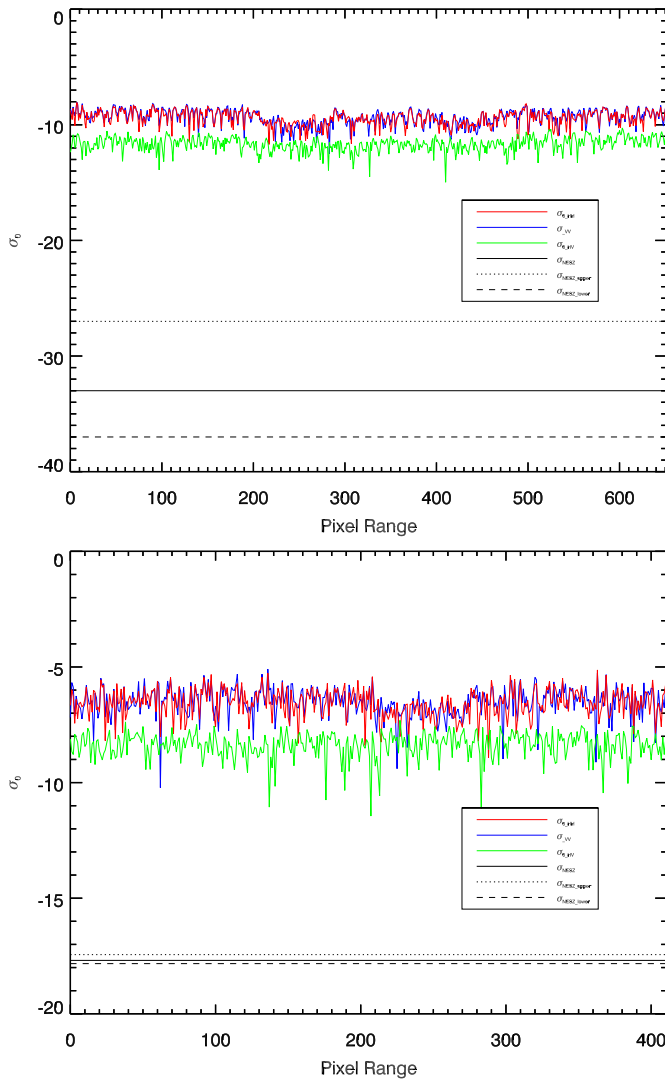
Fig. 2. Top: σ^o values of the transact shown with red line on Fig. 3 RADARSAT-2 acquisition. Bottom: σ^o values of the transact shown with red line on Fig. 4 TerraSAR-X acquisition. Solid black line indicates the average *NESZ*, dotted and dashed black lines indicate upper and lower bound of the noise floor respectively.

fully polarimetric X-band SAR data have been acquired by TerraSAR-X and TanDEM-X constellation during a scientific exploration campaign started in October 2014 and continued until March 2016. One of the main objectives of this campaign is to evaluate quad-polarized X-band high resolution SAR data to develop new technologies and applications. X-band quad pol data were acquired using Dual Receive Antenna (DRA) configuration mode. DRA configuration is achieved by electronically splitting the physical antenna (4.8 m in Azimuth) during receive into two parts separated in along track (Mittermayer and Runge, 2003; Eineder and Fritz, 2006). Therefore, in order to obtain the full scattering matrix the whole antenna is transmitting one polarization (toggled pulse by pulse to transmit two polarization) and in reception. The split of the antenna enables recording of two polarizations (Breit et al., 2010). The X-band fully polarimetric data which were acquired over the study area is quite unique, as currently only the TerraSAR-X and TanDEM-X constellation is able to provide such space-borne observations (only during science phase). On the other hand C-band RADARSAT-2 Quad pol SAR data is available in two different modes, Standard Quad pol and Fine Quad Pol. In both quad polarization modes, a nominal image scene covers an area of approximately 25 km (Range) × 25 km (Azimuth). These two modes of quad pol data is also

available in 'Wide' mode, where a nominal image scene covers an area of approximately 50 km (Range) × 25 km (Azimuth). In case of TerraSAR-X StripMap quad polarization mode, a nominal image scene covers an area of approximately 16 km (Range) × 55 km (Azimuth).

All of the images acquired were Single-Look Complex (SLC) products with nominal slant range resolution of approximately 1.2 m in case of TerraSAR-X StripMAP and 5.2 m in case of RADARSAT-2 Fine Quad (FQ) and Fine Quad Wide (FQW) which is ideal for monitoring offshore platform clusters like Bombay High. Fig. 1 shows the location of the study area, platform locations and an overview of the acquired TS-X images. The dataset includes different beams of TerraSAR-X StripMAP mode (e.g. StripFar_006, StripNear_009 etc.) and RADARSAT-2 Fine Quad pol Mode (e.g. FQ10, FQ13, FQ6W etc.) incorporating a broad range of incidence angles, from 20 to 35 degree. The incidence angle range was chosen due to its low instrument noise floor, approximate NESZ range [−17 dB to −26 dB] in case of TerraSAR-X DRA StripMAP and −35.0 ± 4 dB in case of RADARSAT-2 Fine Quad and −33.0 ± 6 dB in case of RADARSAT-2 Fine Quad Wide) which is a critical parameter in respect to the polarimetric system performance and low enough for dark feature observation even at low wind conditions (Zhang et al., 2011; Velotto et al., 2011; Latini et al., 2016). It is important to note that the NESZ range provided here holds for TS-X data acquired in DRA mode and has been extracted from the particular dataset used in this study. Fig. 2 represent the σ^o values of a transact line over clean water and oil spill spots, which clearly shows that the σ^o values are well above the respective *NESZ* values for both sensors. The dataset is strongly heterogeneous, contains several oil spill spots, providing fresh and old platform sourced spills and incorporating different wind conditions. All the TS-X and RS-2 images present in the dataset were in the range of desirable wind conditions which is around 3–13 m/s. Moreover, the dataset contains a comprehensive set of look-alikes, including phenomena such as ship wakes and low wind areas. A small number of look-alike examples present in the dataset are not from the study area and were acquired over either North Sea or Mediterranean Sea.

Fig. 3 shows an example of platform sourced oil spills along with presence of the offshore platform cluster on a RS-2 Fine quad pol wide image acquired on 20th of April 2014 at 01:15 UTC (Ascending orbit) over the study area. Fig. 4 shows an example of a similar platform sourced oil spill on a TS-X StripMap quadpol image acquired few hours before the RS-2 acquisition (Fig. 3) over the same area. As mentioned earlier, some of the look-alike examples were collected outside of the study area as occurrences of look-alikes over the study area are very rare. Fig. 5 demonstrates manifestations of a weather induced look-alike phenomenon on the RS-2 Fine quad pol wide image acquired over the Balearic Sea, near the coast of Barcelona on 30th November 2012 at 17:43 UTC. An example of look-alike manifestations due to presence of algae bloom on a TS-X StripMap quad pol image is presented in Fig. 13.

3. Polarimetric features

In case of fully polarimetric SAR acquisition, the scattering matrix is given as

$$S = \begin{bmatrix} S_{HH} & S_{HV} \\ S_{VH} & S_{VV} \end{bmatrix} \qquad (1)$$

where $S_{XX} = |S_{XX}| \exp(j\phi_{XX})$, with $|S_{XX}|$ represents the amplitude and ϕ_{XX} represents the phase of the complex scattering coefficient. The spatial averaging window size was chosen to be 11 pixels for our sample dataset throughout this publication.) The scattering vector is commonly analyzed with respect to the lexicographic basis and the Pauli basis. The resulting scattering matrices (averaged covariances) are the well-
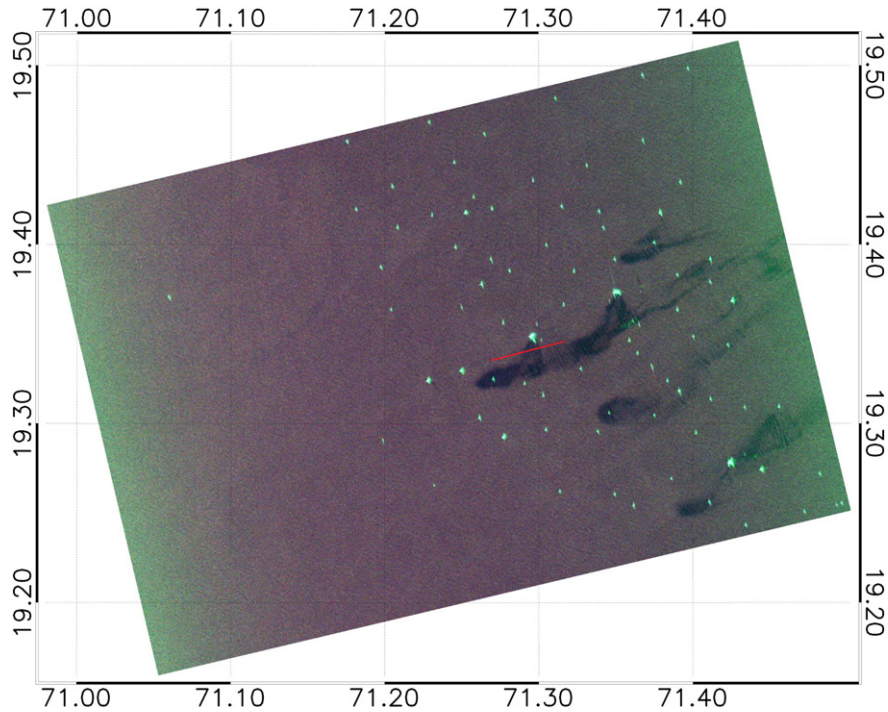
Fig. 3. RADARSAT-2 Quad polarimetric image represented in Pauli RGB (Mid incidence angle: $\theta = 25.4$, beam mode: FQ6W) acquired on 02nd of June 2015 at 13:16 UTC (Ascending Orbit) over Bombay High offshore platform cluster. This image is a part of the training dataset. (© MDA, 2015).

known coherency matrix T_3 and covariance matrix S_3:

$$T_3 = \frac{1}{\sqrt{2}} \begin{pmatrix} \langle |S_{HH} + S_{VV}|^2 \rangle & \langle (S_{HH} + S_{VV})(S_{HH} + S_{VV})^* \rangle & \langle (S_{HH} + S_{VV})(2S_{HV})^* \rangle \\ \langle (S_{HH} + S_{VV})^*(S_{HH} + S_{VV}) \rangle & \langle |S_{HH} + S_{VV}|^2 \rangle & \langle (S_{HH} - S_{VV})(2S_{HV})^* \rangle \\ \langle (S_{HH} + S_{VV})^*(2S_{HV}) \rangle & \langle (S_{HH} + S_{VV})^*(2S_{HV}) \rangle & \langle |(2S_{VV})|^2 \rangle \end{pmatrix} \tag{2}$$

$$S_3 = \begin{pmatrix} \langle |S_{HH}|^2 \rangle & \langle (S_{HH})(S_{VV})^* \rangle & \langle (S_{HH})(S_{HV})^* \rangle \\ \langle (S_{HH})^*(S_{VV}) \rangle & \langle |S_{VV}|^2 \rangle & \langle (S_{VV})(S_{HV})^* \rangle \\ \langle (S_{HH})^*(S_{HV}) \rangle & \langle (S_{VV})^*(S_{HV}) \rangle & \langle |S_{HV}|^2 \rangle \end{pmatrix} \tag{3}$$

The concept for using Polarimetric SAR (PolSAR) data for oil slick observation was initially assessed in Gade et al. (1998) and later on in Migliaccio et al. (2007) for SIR-C/X-SAR data followed by an experimental demonstration on fully polarimetric ALOS PALSAR data in [17]. The principal concept was then adapted for X-band by Velotto et al. (2011), using TerraSAR-X dual pol coherent Single Look Complex (SLC) data. The polarimetric electromagnetic model, which is the basis of this proposed methodology predicts that the sea surface is governed by Bragg scattering (or tilted-Bragg scattering), has a high inter-channel (co-pol) correlation (see Eq. (6)), and in case of non-Bragg scatter (e.g. oil covered sea surface) the correlation is significantly lower (Velotto et al., 2011; Skrunes et al., 2014a). In (Velotto et al., 2011) the authors demonstrated that the standard deviation of Co-polarized Phase Difference (CPD) for a polluted area is significantly higher compared to pollution free background due to significant deviation from Bragg scattering mechanism and on the other hand lower coherence for polluted area due to the same reason. In Migliaccio et al. (2007, 2009b), Velotto et al. (2011), Skrunes et al. (2014b) the model has been demonstrated to be congruent even at different frequencies, L-, C- X-band making it attractive for further evaluation. CPD has a probability distribution (pdf) that depends on the number of looks $\updownarrow$ ($\updownarrow=1$ in both cases of TS-X and RS-2 dataset)

and co-polarized phase difference(CPD) is given by

$$CPD = \varphi_{HH} - \varphi_{VV}, \tag{4}$$

and standard deviation of CPD is denoted by $\sigma_{\varphi_{co}}$

$$\sigma_{\varphi_{co}} = StdDev(CPD). \tag{5}$$

When HH and VV are uncorrelated (in case of an oil covered surface), the pdf becomes uniformly distributed between -180 and 180.

The complex correlation coefficient between HH and VV (ρ_{CO}) is given in Eq. (6), where * denotes complex conjugate and $\langle \cdot \rangle$ denotes spatial averaging.

$$\rho_{CO} = \frac{|\langle S_{HH} S_{VV}^* \rangle|}{\sqrt{\langle S_{HH} S_{HH}^* \rangle \langle S_{VV} S_{VV}^* \rangle}}. \tag{6}$$

In Migliaccio et al. (2007), well-known Eigenvalue decomposition is proposed for use in oil spill detection algorithms. Eigenvalue based polarmetric features i.e., entropy (H), anisotropy (A) and mean scattering angle (α) (Cloude and Pottier, 1996, 1997; Hajnsek et al., 2003) are used with a combination of constant false alarm rate (CFAR) filter for oil spill classification on a single SIR-C/X-SAR L-band data set. In a polarimetric approach one generally first computes the (locally averaged) covariance matrix of the scattering vector in order to compute the Eigenvalues.

The (quad-polarimetric) eigenvalues λ_1, λ_2, and λ_3 of T_3 are used to compute $p_j = \lambda_j/(\lambda_1 + \lambda_2 + \lambda_3)$. This is the input for deriving entropy

$$H = -(p_1 \log_3(p_1) + p_2 \log_3(p_2) + p_3 \log_3(p_3)), \tag{7}$$

and

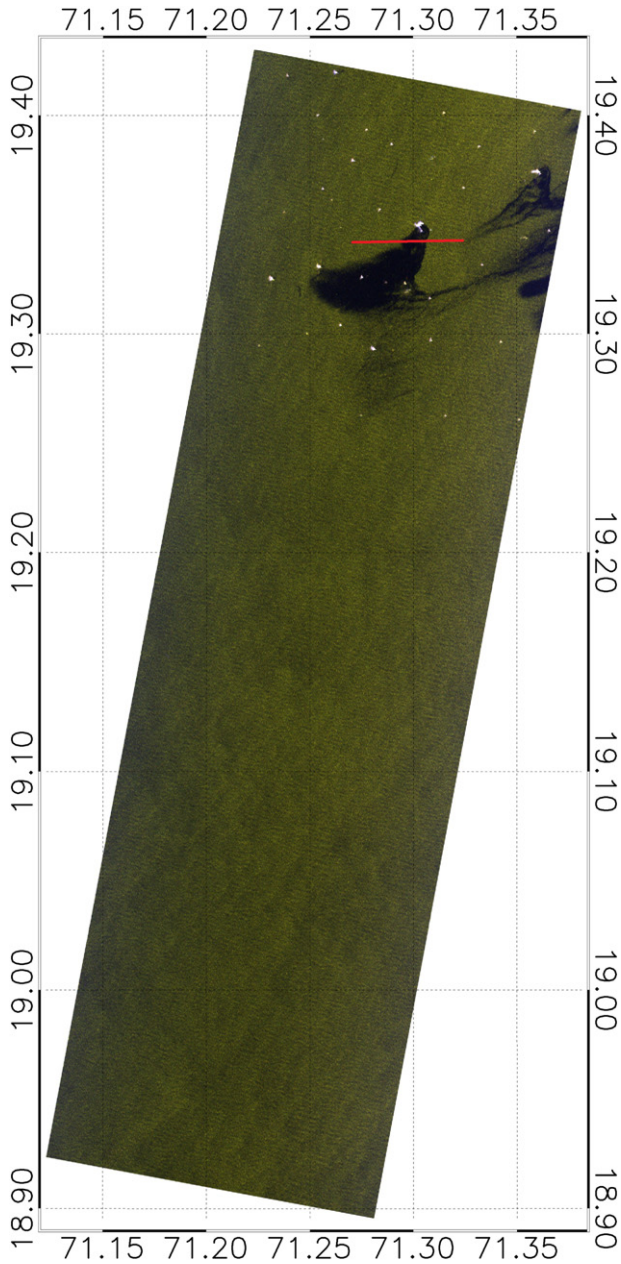$$A = \frac{(p_2 - p_3)}{(p_2 + p_3)} \tag{8}$$

Fig. 4. TerraSAR-X Quad polarimetric image represented in false color composite (mid incidence angle $\theta = 29.63$) StripMAP (stripFar_006) acquired on 01st of June 2015 at 01:15 UTC (Descending Orbit) over Bombay High offshore platform cluster. This image is a part of the training dataset. (© DLR,2015).

From the eigenvectors v_1, v_2 and v_3 of T_3 one obtains

$$\alpha_i = \arccos(v_j(1)), j = 1, 2, 3. \tag{9}$$

The average α angle we define by

$$\alpha = \alpha_1 p_1 + \alpha_2 p_2 + \alpha_3 p_3 \tag{10}$$

While the classical $H - A - \alpha$ parameters (cf. Cloude and Pottier, 1997) in the fully polarimetric case also permit the physical interpretation (eg. regarding predominant scattering mechanisms and values between 0 and 1), we do not further explore this aspect for our two-dimensional adaptation. In case of an oil covered sea surface, H tends to zero, indicating therefore a dominant scattering mechanism scenario. On the other hand, a pollution free sea surface dominated by relatively

high *Entropy* represents random scattering mechanisms. Entropy has also been found useful for oil spill detection on ALOS PALSAR polarimetric data in Migliaccio et al. (2009a). In Liu et al. (2011), authors also used a combination of Cloude-Pottier based decomposition features ($H - A - \alpha$) along with the co-pol correlation coefficient (ρ_{CO}) in order to form a feature combination to enhance oil spill detection capability on UAVSAR L-band fully polarimetric data. In addition to that, Polarimetric *Span* is also investigated as a separate feature in that study. Polarimetric *Span* can be derived from the summation of Eigenvalues, therefore in the fully polarimetric case it is given by

$$Span = \lambda_1 + \lambda_2 + \lambda_3. \tag{11}$$

As we discussed in this section, many previous studies examined different polarimetric features specially co-polarized phase difference (φ_{CO}) and $H - A - \alpha$ for oil spill discrimination and characterization. Nonetheless, reliability of a single polarimetric feature for oil spill and look-alike discrimination has still not been adequately answered. Fig. 6 presents histograms of co-polarized phase difference (φ_{CO}) and $H - A - \alpha$ values which are extracted from RS-2 imagery for four different classes i.e. Crude Oil (CO), Emulsion (EM), Look-Alike (LA) and Open Water (OW). Crude Oil (CO), Emulsion (EM) and Open Water (OW) histograms were obtained using a well-known RS-2 Fine Quad Pol image presented in Fig. 3a in Skrunes et al. (2014b) and Look-Alike (LA) histograms were obtained using Fig. 5. It can be observed from 6 that in case of co-polarized phase difference (φ_{CO}) Crude Oil and Look-alike have a very similar distribution. On the other hand it is a relatively trivial task to discriminate Emulsion from Crude oil and look-alike using co-polarized phase difference (φ_{CO}). In case of Entropy (H), Emulsion and Open Water exhibit similar characteristics whereas Emulsion and Look-alike show a large difference. Therefore it is evident from Fig. 6 that only one polarimetric feature will be insufficient to discriminate different types of look-alike and oil spills which is also valid for TS-X observations. Therefore we propose a methodology which uses a combination of well-known and recently established polarimetric features to characterize dark spots. In addition to well-known polarimetric features we also investigate an array of additional polarimetric features which are relatively under exploited for oil spill detection and characterization purpose.

A recent study by Skrunes et al. (2014b) evaluated eight established polarimetric features on two C-band RADARSAT-2 fine quad pol data where only HH and VV channels were taken into account. In that study, geometric intensity was based on the T_2 matrix whereas, in the present study geometric intensity μ is expressed as,

$$\mu = \det(T_3)^{1/2} \tag{12}$$

is used as a feature parameter based on the T_3 coherency matrix. Another recent study by Singha et al. (2016) also found μ to be useful for object-based oil spill and look-alike discrimination. In addition to the T_3 matrix based features, $\sigma_{\varphi_{co}}$ and ρ_{CO}, another lexicographic based feature, and the real part of the co-polarization cross product (Rco) were evaluated in Skrunes et al. (2014b).

The real part of the co-polarization cross product (Rco) is given by

$$Rco = |\Re(\langle S_{HH} S_{VV}^* \rangle)| \tag{13}$$

where $\Re$ stands for real part and

$$\langle S_{HH} S_{VV}^* \rangle = \left\langle |S_{HH}||S_{VV}| e^{i(\varphi_{HH} - \varphi_{VV})} \right\rangle \tag{14}$$

Rco is used for oil spill and look-alike discrimination in Nunziata et al. (2008) (also in Migliaccio et al., 2009a) as main part of a processing chain, where oil spills are distinguished from clean sea and biogenic look-alikes with the help of the ratio between Rco and $\langle |S_{HV}^2| \rangle$. In Nunziata et al. (2008) authors described the physical rationale behind
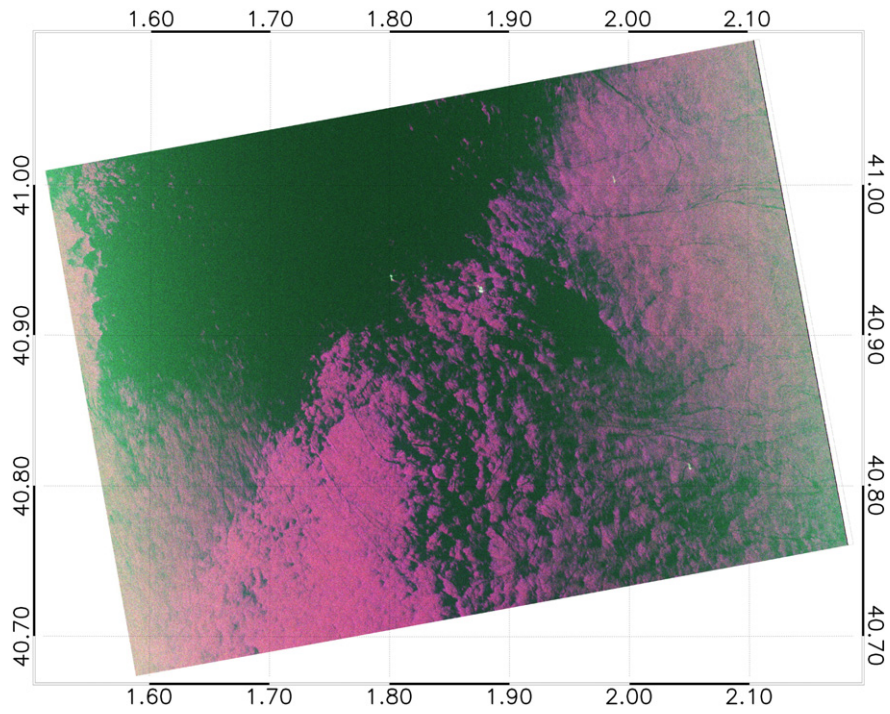
Fig. 5. Manifestation of a weather induced 'look-alike' phenomenon on RADARSAT-2 Quad polarimetric image represented in Pauli RGB (Mid incidence angle: $\theta = 30.00$, beam mode: FQ10W) acquired on 30th November 2012 at 17:43 UTC (Ascending Orbit) over the Balearic Sea, near the coast of Barcelona. This image is a part of the training dataset. (© MDA, 2015).
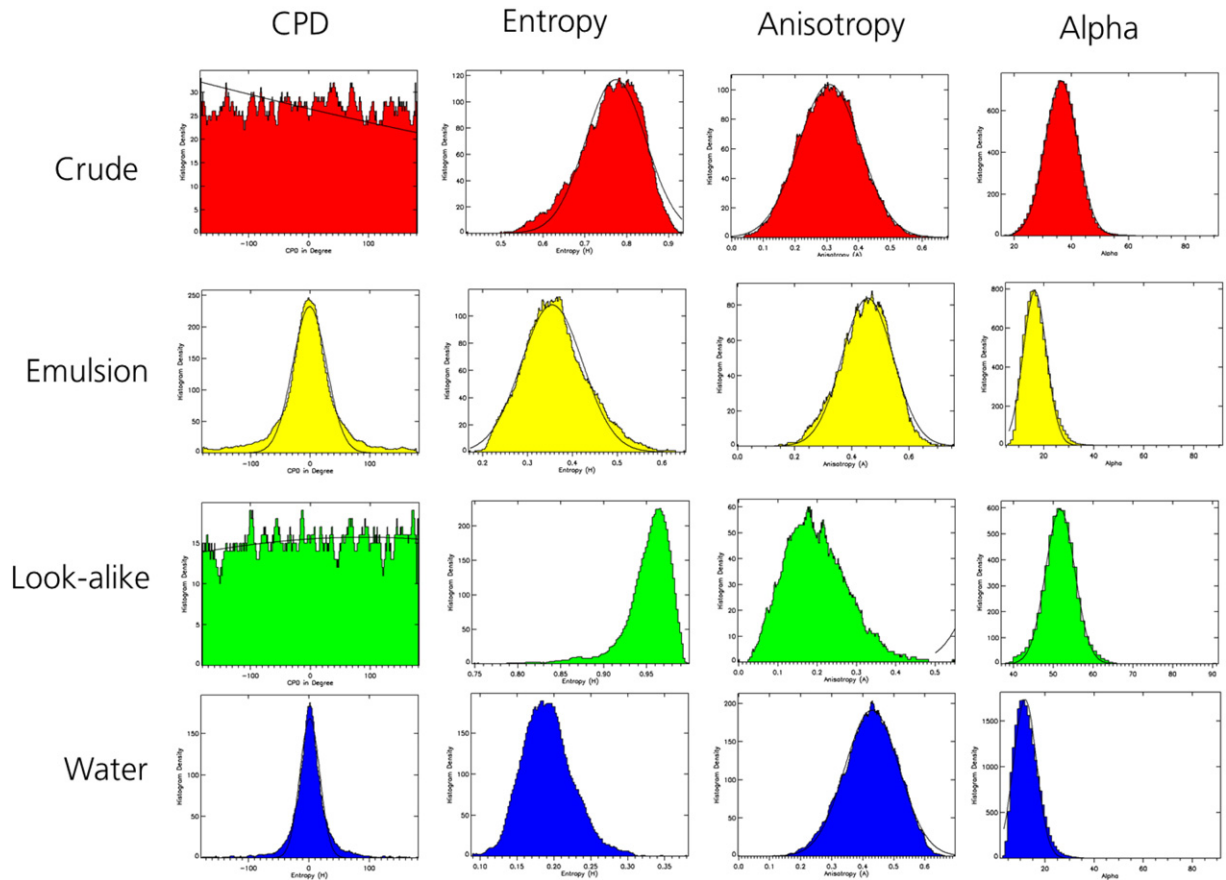

Fig. 6. Polarimetric feature histogram for Crude Oil (CO), Emulsion (EM), Look-Alike (LA) and Open Water (OW) extracted from RADARSAT-2 Quadpol image. Polarimetric features (from left to right): Copolarization phase difference, *CPD*, Entropy, *H*. Anisotropy, *A*. Alpha, α.

Table 1

TerraSAR-X and RADARSAT-2 imaging modes used in this study.

Sensor	Incidence angle range	Polarization mode	Imaging mode	Slant Rng Res. (m)	Az Res. (m)
TerraSAR-X	29°–38°	Quad-Pol(DRA[*])	StripMAP	1.2 m	6 m
RADARSAT-2	22°–48°	Quad-Pol	Fine Quad	5.2 m	7.6 m
RADARSAT-2	22°–48°	Quad-Pol	Fine Quad Wide	5.2 m	7.6 m

[*] DRA - Dual Receive Antenna (Experimental Mode).

Table 2

List of polarimetric features used in this study.

Polarimetric features
Stddev Co-Pol Phase Difference, $\sigma_{\varphi_{co}}$ Velotto et al. (2011), Migliaccio et al. (2009b)
Coherency Coefficient, ρ_{co} Velotto et al. (2011)
Geometric Intensity, μ Skrunes et al. (2014b)
Real Part Co-Pol Cross Product, Rco Migliaccio et al. (2009b)
Entropy, H Zhang et al. (2011), Liu et al. (2011), Skrunes et al. (2014b)
Anisotropy, A Skrunes et al. (2014b), Liu et al. (2011)
Alpha angle, α Zhang et al. (2011), Liu et al. (2011), Skrunes et al. (2014b)
Scattering Diversity, δ Praks et al. (2009)
Surface Scattering Fraction, τ Praks et al. (2009)
Polarimetric, $Span$ Liu et al. (2011), Singha et al. (2016)

this fact, wherein a sea surface that is covered with biogenic look-alikes is still dominated by Bragg scattering, hence indistinguishable from clear background. In case of an oil covered area the value of Rco is expected to be nearly zero and in case of a clear background Rco is expected to have a value greater than zero (Nunziata et al., 2008).

In addition to those established polarimetric feature we also exploit two new coherency matrix (T_3) based features (invariant to unitary transforms), namely Scattering diversity and Surface scattering fraction for oil spill detection and characterization, previously proposed by Praks et al. (2009). Praks et al. (2009) shows that Scattering diversity combined with the surface scattering fraction can be used to form a classification space almost identical to the traditional Entropy-Alpha classification space (Cloude and Pottier, 1997). Our motivation of introducing these two parameters was these features are very straightforward to calculate and require less time to compute compared to traditional $H - A - \alpha$. These two features are proven to be useful for other maritime related applications such as sea ice classification (Ressel and Singha, 2016). However, until now those two features have not been exploited for oil spill and look-alike characterization.

Scattering diversity is defined as

$$\delta = \frac{3}{2}\left(1 - \left(\frac{\|T_3\|_F}{span^{(q)}}\right)^2\right), \tag{15}$$

(where $\|T_3\|_F$ denotes the T_3 Frobenius norm). Surface scattering fraction is defined as

$$\tau = \frac{\left\langle |S_{HH} + S_{VV}|^2\right\rangle}{span}. \tag{16}$$

All of the features used in this study are given in Table 2 and illustrated in Fig. 7 for an example of platform sourced oil pollution on a RS-2 fully polarimetric image. Figs. 8 and 9 show examples of platform sourced oil pollution and look-alike on TS-X fully polarimetric imagery, respectively. (See Table 1 for further details.)
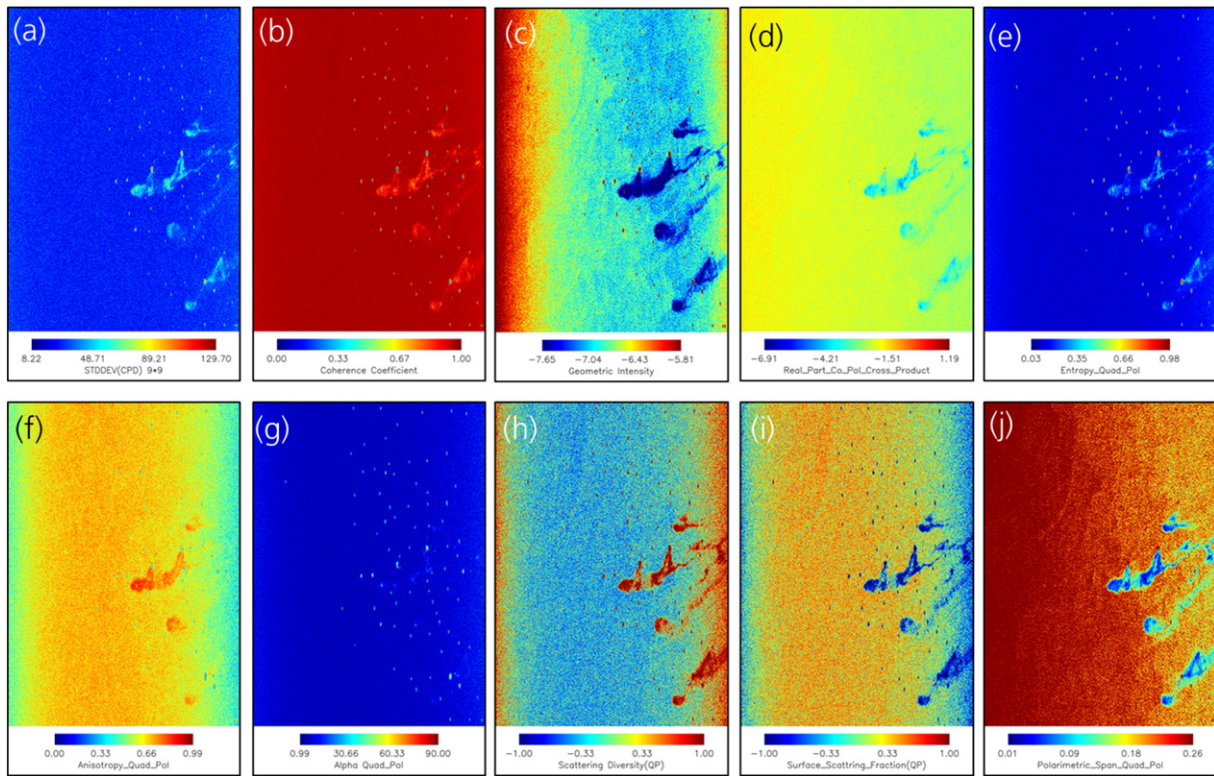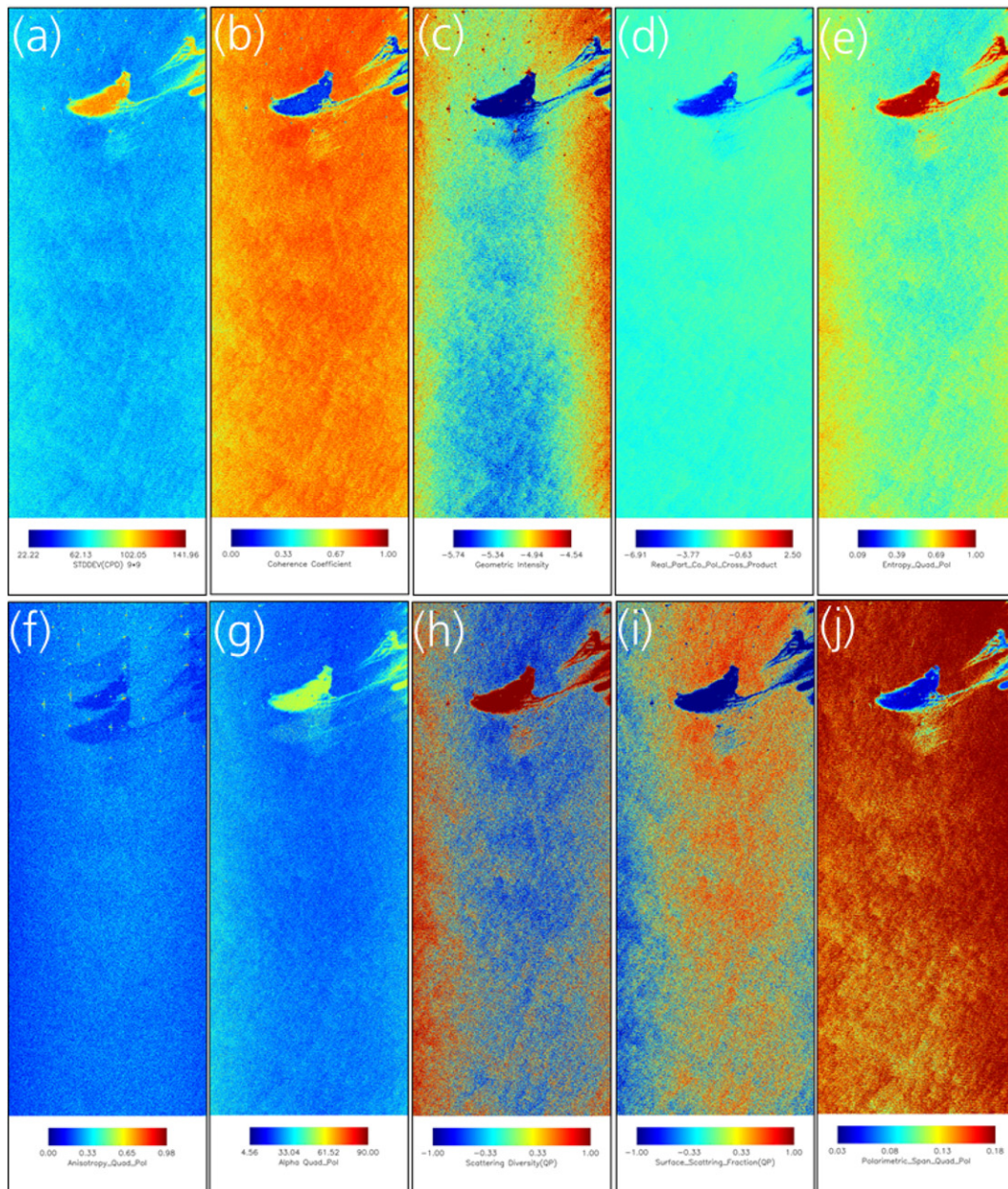

Fig. 7. Polarimetric features extracted from RADARSAT-2 Quadpol image presented in Fig. 3. (a) Standard deviation of copolarization phase difference, $\sigma_{\varphi_{co}}$. (b) Magnitude of Coherence Coefficient, ρ_{co}. (c) Geometric intensity, $\log(\mu)$. (d) Real part of the copolarization cross product, $(\log(r_{co}))$. (e) Entropy, H. (f) Anisotropy, A. (g) Alpha angle, α. (h) Surface scattering diversity, δ. (i) Surface Scattering Fraction, τ. (j) Polarimetric $Span$. The features μ, r_{co} are log transformed for visualization purpose (© DLR, 2015).

Fig. 8. Polarimetric features extracted from TerraSAR-X Quadpol image presented in Fig. 13. (a) Standard deviation of copolarization phase difference, $\sigma_{\varphi_{co}}$, (b) Magnitude of Coherence Coefficient, ρ_{CO}. (c) Geometric intensity, $\log(\mu)$. (d) Real part of the copolarization cross product, $(\log(r_{CO}))$. (e) Entropy, H. (f) Anisotropy, A. (g) Alpha angle, α. (h) Surface scattering diversity, δ. (i) Surface Scattering Fraction, τ. (j) Polarimetric *Span*. The features μ, r_{CO} are log transformed for visualization purpose (© DLR, 2015).

4. Methodology

4.1. Neural network classification

As mentioned in the introduction, we performed a pixel-based supervised classification using an Artificial Neural Network (ANN). The training dataset was extracted from 5 TS-X and 4 RS-2 images for four separate classes, Crude Oil (CO), Emulsion (EM), Look-Alike (LA) and Open Water (OW) incorporating different incidence angles. From the initial training dataset, 20% of the samples had been reserved for testing purpose. It is important to note that the training and testing datasets are mutually exclusive and some samples of the training (testing) dataset (RS-2) were extracted form verified Crude Oil (CO), Emulsion (EM), Look-Alike (LA) spots, previously presented and studied by Skrunes et al. (2014b, 2014a). A limited amount of training samples for CO (X-band) was collected from platform sourced fresh spills (with higher dampening ratio compared to EM samples). LA samples include a broad range of phenomena incorporating lower dampening (plant oil) and higher dampening (weather induced phenomenons, algae blooms) effects. The rest of the images, i.e. 15 TS-X and 16 RS-2, were treated as validation dataset, thus disjoint from the training (testing) dataset. The feature set we used contained all features and their respective local variances, which was computed for each center pixel of an 11×11 sub-matrix sliding over the entire feature image. Therefore, we extracted for each pixel mentioned polarimetric features (along with their local variances) and then ingested the feature vectors into the classifier. The implementation was carried out both in the Exelis IDL programming language (Image ingestion, calibration, feature extraction, statistical analysis) and in C (FANN library classifier, Nissen, 2005). The hardware specifications used were: 11 GB RAM, 2.7 *Ghz* Intel Core i-7 3740 QM, virtual linux OS.

The validation of the trained classifier were carried out on rest of the TS-X and RS-2 images i.e. 15 TerraSAR-X and 16 RS-2 images. It is
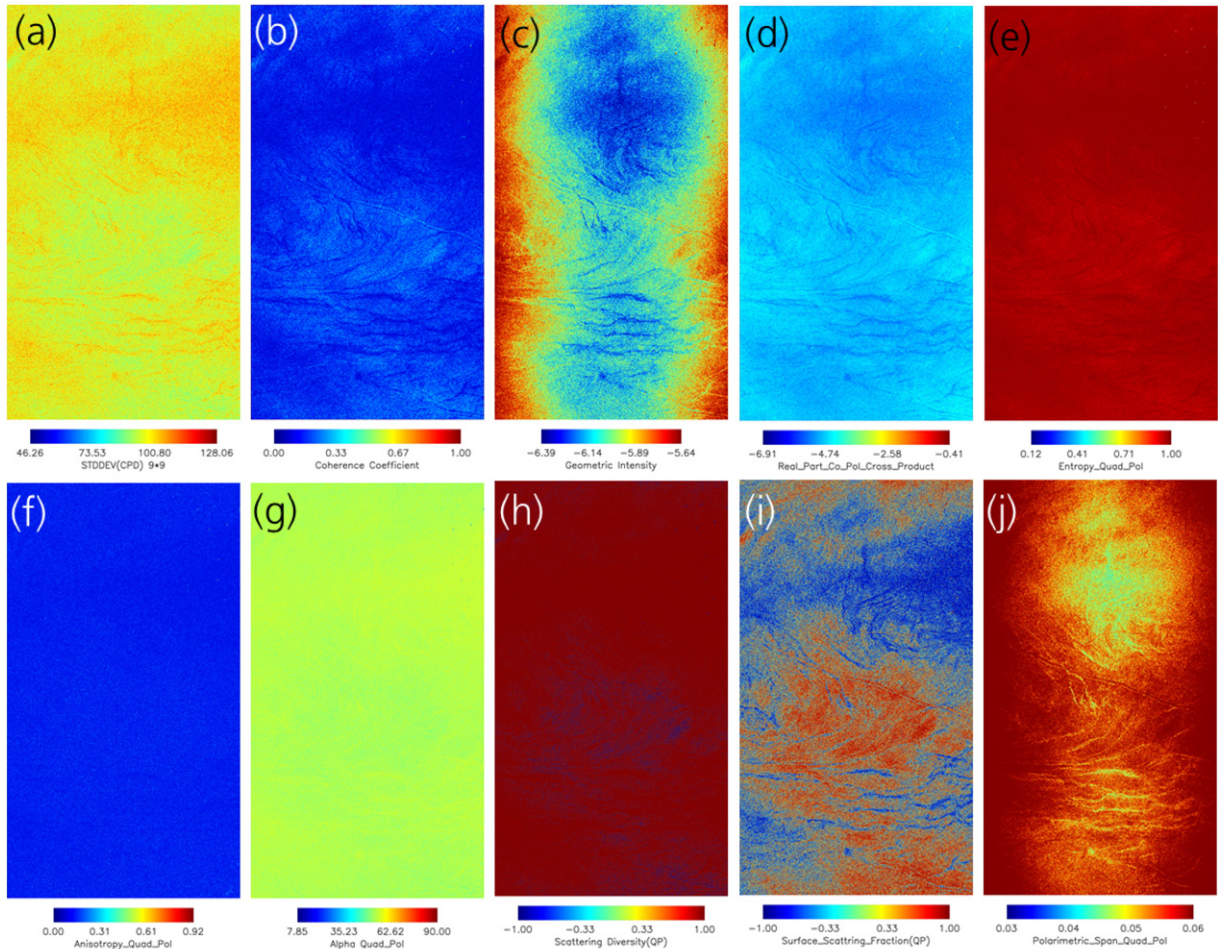
Fig. 9. Polarimetric features extracted from TerraSAR-X Quadpol image presented in Fig. 13. (a) Standard deviation of copolarization phase difference, $\sigma_{\varphi_{co}}$. (b) Magnitude of Coherence Coefficient, ρ_{CO}. (c) Geometric intensity, $\log(\mu)$. (d) Real part of the copolarization cross product, $(\log(r_{CO}))$. (e) Entropy, H. (f) Anisotropy, A. (g) Alpha angle, α. (h) Surface scattering diversity, δ. (i) Surface Scattering Fraction, τ. (j) Polarimetric *Span*. The features μ, r_{CO} are log transformed for visualization purpose (© DLR, 2015).

important to note here that the images present in the validation dataset are mutually exclusive with the training a testing dataset. A detailed description of the results and discussion about the discriminative power for each polarimetric features are presented in Section 5 along with some examples of detected oil spill and look alike for both frequency bands.

4.2. Mutual information for feature selection

As mentioned earlier, in addition to classification accuracy assessment we have also carried out mutual information analysis of the extracted features to assess their contribution to the classification process. Let X, Y be two random variables (with joint and marginal densities, no point masses). Then the mutual information $\mathcal{T}$ of X and Y is

defined to be

$$\mathcal{T}(X|Y) = \mathcal{H}(X) - \mathcal{H}(X|Y), \tag{17}$$

where $\mathcal{H}(\mathcal{X})$ denotes the entropy and $\mathcal{H}(X|Y)$ denotes the conditional entropy of X given Y. A detailed introduction can be found in Yu and Liu (2003), Peng et al. (2005) and its usage for remote sensing applications in Ressel and Singha (2016). The intuition of this definition of mutual information $\mathcal{T}$ is to describe the amount of information that is shared by both feature variable, X and Y, i.e. their "information overlap". In other words, the higher the $\mathcal{T}(X|Y)$ value is, the more reliably one can make a prediction about X from available knowledge of Y. By such a definition, one can quantify, in terms of information theory, the (nonlinear) information correlation of X and Y. Classical statistical correlation can only indicate linear relationships, thus mutual information can be considered a

Table 3
Classification results compared to reference data samples from each class, averaged over different neural network topologies, RS-2 dataset.

ANN classification	Reference class			
	OS	EM	LA	OW
OS	100.0%	0%	0%	0%
EM	0%	96.2%	0%	0%
LA	0%	0%	99.0%	2.7%
OW	0%	3.8%	1.0%	97.3%

Table 4
Classification results compared to reference data samples from each class, averaged over different neural network topologies, TS-X dataset.

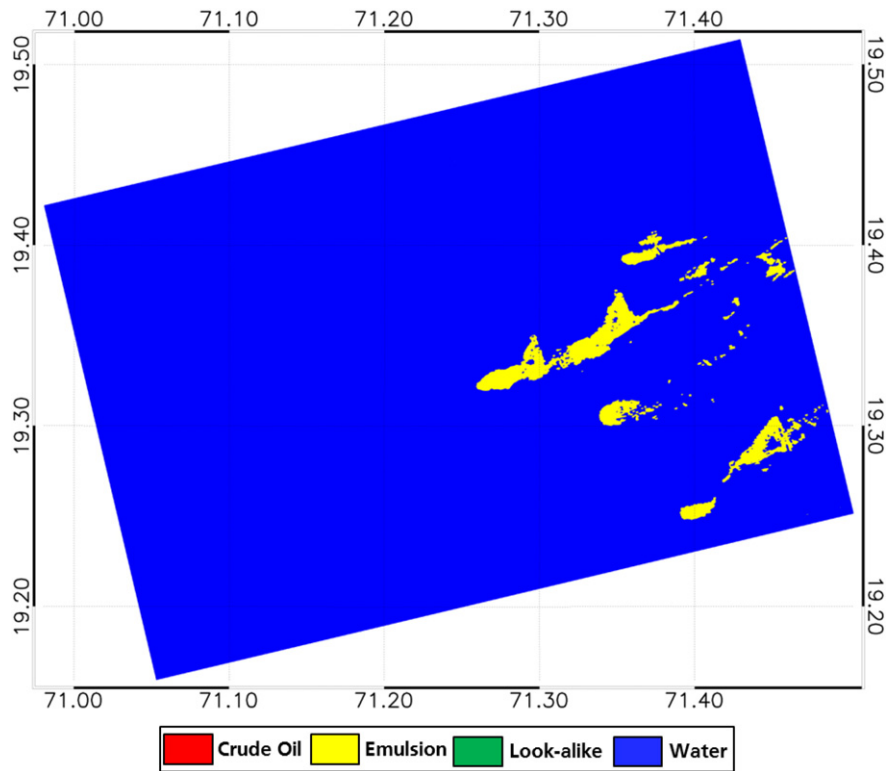| ANN classification	Reference Class			
	OS	EM	LA	OW
OS	100.0%	0%	0%	0%
EM	0%	95.4%	0%	0%
LA	0%	0%	99.3%	3.8%
OW	0%	4.6%	0.7%	96.2%

Fig. 10. Example of detected oil (Type:Emulsion) on a RADARSAT-2 Quadpol image, presented in Fig. 3.

generalization of classical correlation (see e.g. Lange and Grubmüller, 2006). According to this intuition of "shared information", one would expect $\mathscr{T}$ to be symmetric in X and Y, and this indeed holds also for the rigorous mathematical sense, i.e., $\mathscr{T}(X|Y) = \mathscr{T}(Y|X)$. Since we are mainly interested in relative feature quality, we will only use $\mathscr{T}$ to rank features relatively and not make further use of the absolute values of $\mathscr{T}$.

In our analysis, we will use the following terminology concerning particular choices of X and Y: When Y is a feature and X is the class information (X attains e.g. CO, EM, LA and OW), a (relatively) high mutual information $\mathscr{T}$ would indicate a high predictive value of feature Y for determining the class X. And by the symmetry of $\mathscr{T}$, information on X permits to make a prediction of corresponding values of Y. The configuration (Y feature, X all classes) we use to rank the features according to relevance (all-class-relevance). We will write $\mathscr{T}(Y|Class(all))$ for this situation. When in computing $\mathscr{T}(Y|X)$ we use reference data only from two classes, i.e. X assumes only two values of class property, then the resulting value $\mathscr{T}(Y|X)$ for a feature Y is called the two-class relevance of feature Y.

In another configuration, we let X and Y be two different features. When $\mathscr{T}(X|Class(all))$ and $\mathscr{T}(Y|Class(all))$ are about equal (i.e., have equal relevance), high mutual information $\mathscr{T}(X|Y)$ then indicates redundancy of the two features X and Y. Such redundancy analysis may serve in operational streamlining of the algorithm by discarding those features that are found to be redundant. In order to obtain a higher comparability, $\mathscr{T}(X|Y)$ is normalized by $\sqrt{\mathscr{H}(X).\mathscr{H}(Y)}$ (see Strehl and Ghosh, 2003).

Into order to adapt the feature values to our particular choice of neural network, all features are rescaled into the range [−1.0,1.0]. We use the common nonlinear rescaling method involving the tanh function:

$$\tilde{x} = \tanh\left(\frac{x - \overline{X}}{\nu_X}\right), \tag{18}$$

where $\overline{X}$ denotes the mean of all values of feature X in the training data and ν_X denotes the standard deviation of all values of feature X in the training data. Whenever an ANN is trained on data that was rescaled with these particular training data statistical parameters $\mathcal{P} = \{\overline{X}, \nu_X\}$, then all feature vectors ingested into this network for classification need to be rescaled likewise with these parameters $\mathcal{P}$ prior to classification. From now on in this work, we only discuss the rescaled values of the features, since these determine the numerical behavior of our algorithm. The results of our feature analysis will be presented in Subsection 5.2.

5. Results and discussions

5.1. Classification results

As discussed in the Section 4, we train the ANN with a training dataset consisting of ten polarimetric features and their local variances. After training we tested the performance of the trained ANN using a testing dataset (20% of the initial training dataset). Tables 3 and 4 show the classification accuracy achieved by the trained ANN using testing dataset for RS-2 and TS-X respectively. Noting that both training and testing dataset are mutually exclusive and collected from the different images (i.e. different met-oceanic conditions and incidence angle), our approach can be considered to be consistent in itself and stable with respect to different met-oceanic conditions as background. Additionally, the proposed methodology is tuned for operational Near Real Time Services with average processing time of 7–8 min for a RS-2 fine quad pol scene and 10–12 min for a TS-X StripMap quad pol and RS-2 fine quad pol wide scene. This is an essential performance indicator for operational services followed by false positive and false negative rates of the proposed methodology.

In order to demonstrate the reliability of the classifier we show the classified examples of detected oil spills and look-alikes on both RS-2 and TS-X imagery. We first show some examples of classified images,
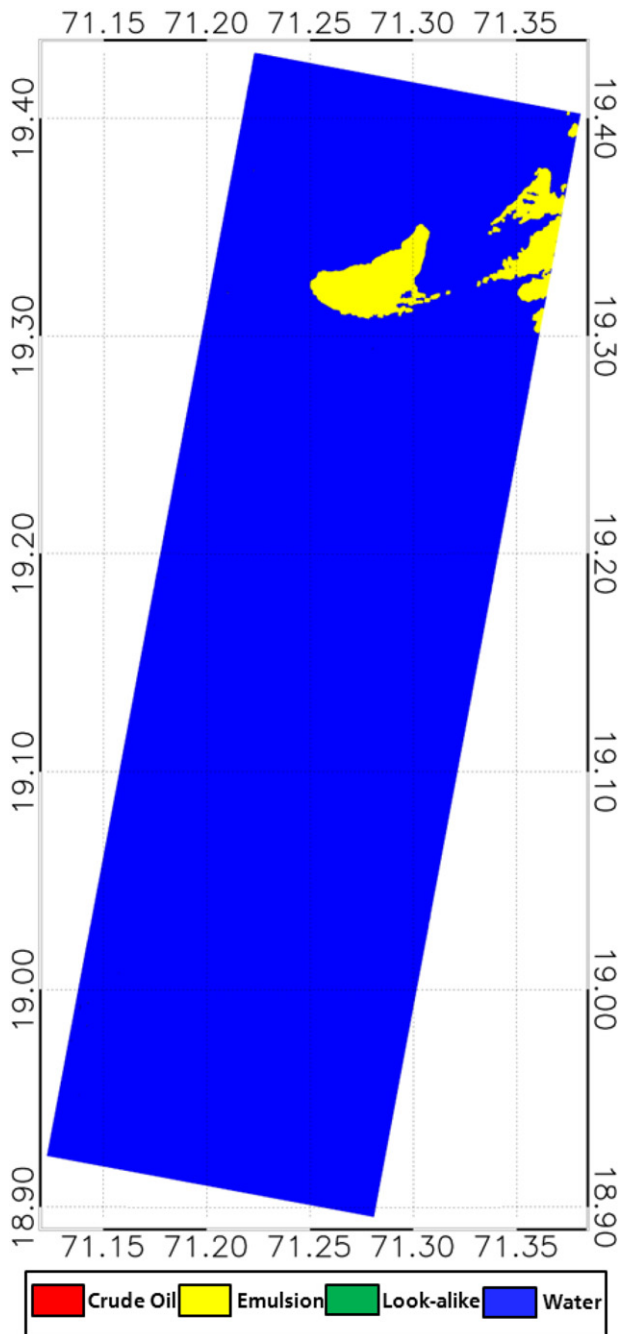
Fig. 11. Example of detected oil (Type:Emulsion) on a TerraSAR-X QuadPol StripMap image, presented in Fig. 4.

wherein the training and testing dataset were gathered followed by examples from the validation dataset.

Fig. 10 shows an example of oil spill on a RS-2 fine quad pol wide imagery acquired on 02nd of June 2015 at 13:16 UTC (See Fig. 3) over the study area where the trained classifier detected the dark-spot as emulsion (EM). Fig. 11 shows an example of an oil spill on a TS-X StripMap quad pol image which was acquired few hours before on 01st of June 2015 at 01:15 UTC over the same area (See Fig. 4). In Fig. 11 the dark-spots also detected as emulsion by the trained classifier for TS-X which is in agreement with the classification results obtained from RS-2 acquisition. As discussed earlier, most important aspect of any oil spill detection methodology is its ability to detect look-alikes on SAR images. In Section 2 we presented an RS-2 fine quad pol wide imagery (See Fig. 5) manifesting the presence of large look-alike spots probably due

to adverse weather conditions. Fig. 12 shows the classified results obtained using the ANN classifier trained for RS-2 where all of the dark-spots are classified look-alikes. Fig. 13 shows occurrences of look-alike phenomena, probably occurring due to an algae bloom on a TS-X quad pol imagery acquired over North Sea during summer 2015. In spite of the image acquired at relatively higher incidence angle (mid incidence angle: $\theta = 38.80$) the ANN classifier, trained for TS-X dataset managed to successfully classify the dark-spots as look-alikes.

To judge visually on the plausibility of the classification on both C and X band SAR imagery, we presented a spatially and temporally coincident RS-2 and TS-X results in Fig. 14 where the TS-X image was acquired on 15th of July 2015 at 01:15 UTC and RS-2 image was acquired within less than one minute after TS-X acquisition. It is important to note here that this dataset is a part of the validation dataset and disjoint from the training and testing dataset. The figure shows two identical oil spills originating from offshore platforms on RS-2 and TS-X imagery. Fig. 14 summarizes that for the locations of recognizably identical oil spills classified as Emulsion (EM) in both frequency bands. We also observe a significant match in the classified oil type (EM) even with a notable difference in incidence angle between TS-X and RS-2 acquisition.

5.2. Relevance and redundancy

From first glance at Table 5, for both sensors we find H and δ to be next to each other in terms of rank and also at the top of the feature list. Both A and α are rather low ranking for both sensors. We also observed that τ and *span* are in the upper half of the table for both TS-X and RS-2. Somewhat different is the relevance of ρ_{CO} which is rather important in TS-X based classification, whereas for RS-2 it scores midrange in terms of relevance. Contribution of *Rco* to the classification process appears to be important for both TS-X and RS-2. When considering only the two-class relevance, we observed for either of the satellites that the five highest ranking features for discriminating two classes are *span*, H, δ, τ, and *Rco* which coincides with what can be observed in Table 5. Another key observation was that the feature $\sigma_{\varphi_{co}}$ ranked lowest or second but lowest, in almost all cases of two-class relevance on both sensors.

The most striking observation in Figs. 15 and 16 is the high correlation of the polarimetric entropy H, and the scattering diversity δ, which fits quite well the theoretical predictions of Praks et al. (2009), III·B and (Ressel et al., 2015; Ressel and Singha, 2016). It is also noticeable from Table 5 that the contribution of μ towards the classification process is higher in case of RS-2 compared to TS-X.

Therefore, we can summarize the most relevant features (the top five features for each class pair and for all-class discrimination) as *span*, τ, δ, *RCO*, and H relevances. Since H and δ carry coinciding information and are of similar relevance, one might consider discarding H. Given that A and α are of inferior relevance for both sensors, we conclude that the eigenvalue based features H, A, α can likely be discarded without worsening the classification result. In particular, this would make the computationally expensive Eigen decomposition dispensable in the processing chain and thus save numerical overhead. Whether this expectation will be met in setting up a classifier with a reduced feature set will be investigated in future studies.

6. Conclusions

A combination of different polarimetric features have exploited to characterize dark spots on C and X-band quad-polarization SAR data using Artificial Neural Network as a classifier. A first analysis of redundancy among these features indicates the directions for further investigation on selection of optimal features combinations (which can help to avoid computational and memory overhead). The contribution of δ, τ and *span* to the classification stage is significant. These features clearly deserve attention in future studies. Additionally, the proposed
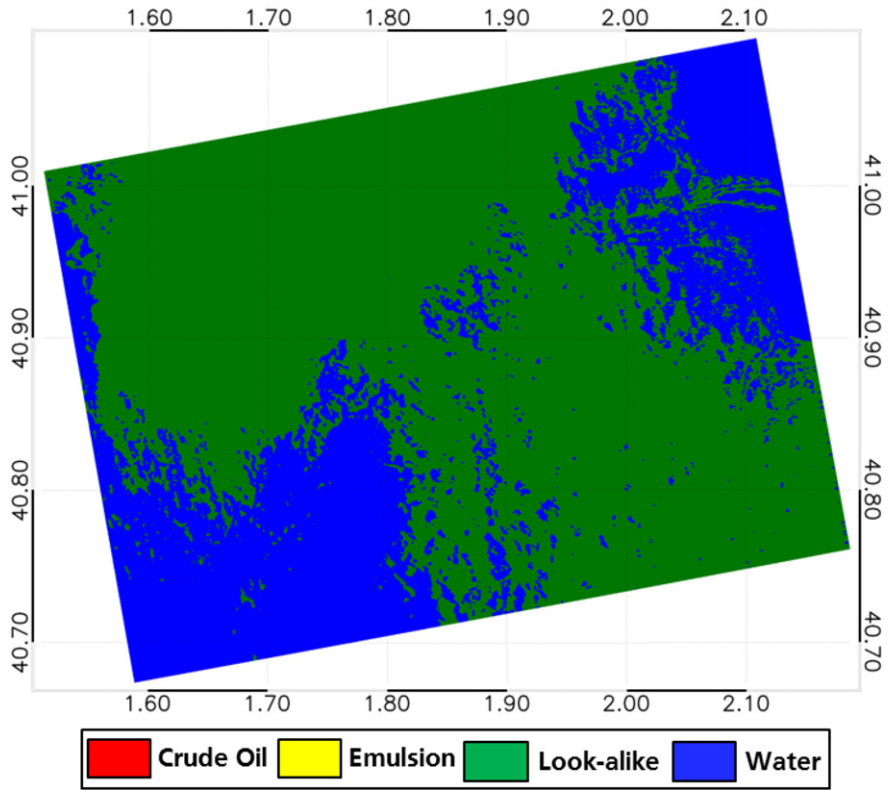
Fig. 12. Example of detected 'look-alikes' (Weather induced) on a RADARSAT-2 QuadPol image, presented in Fig. 5.
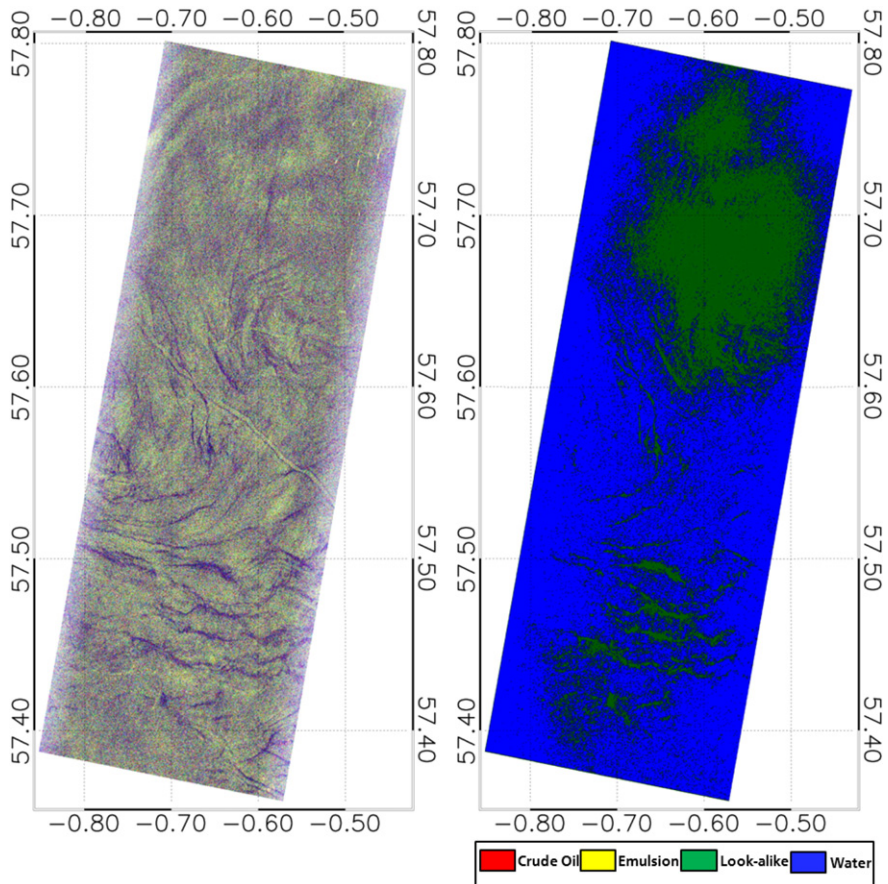

Fig. 13. Left: Manifestation of 'look-alikes' (Algae/Biogenic Slick) on StripMAP image (mid incidence angle: $\theta = 38.80$, stripNear_011, Contrast enhanced) acquired on 13th of July 2015 at 06:24 UTC over NorthSea. Right: Classification result using ANN. (© DLR,2015) This image is a part of validation dataset.
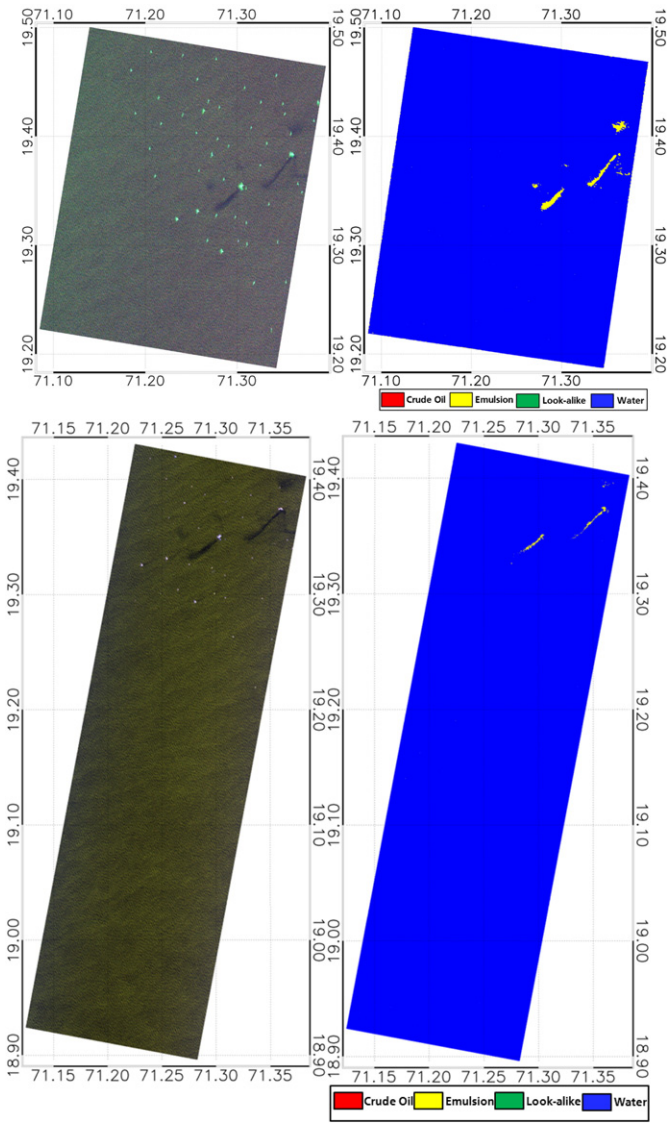
Fig. 14. C and X band fully polarimetric SAR imagery acquired over Bombay High and respective classified imagery. Top left: Pauli representation of RADARSAT-2 Fine Quad Pol Wide (FQ4, mid incidence angle $\theta = 23.2$, Descending Orbit) acquired on 15th of July 2015 at 01:16 UTC (© DLR,2015). Top right: Classified RS-2 image using ANN. Bottom left: TerraSAR-X Quad Pol (Dual Receive Antenna, StripFar_006, mid incidence angle $\theta = 29.3$, Descending Orbit) acquired on 15th of July 2015 at 01:15 UTC (© DLR,2015). Bottom right: Classified TS-X image using ANN. Both images are part of validation dataset.

Table 5
Relevance for distinguishing all different classes (all-class-relevance) in the TS-X training data, and in the RS-2 training data. $\mathscr{T}_{(RS)}$ denotes $\mathscr{T}(X|Class(all))/\sqrt{H(X)}$ for RS-2 data, and $\mathscr{T}_{(TSX)}$ denotes $\mathscr{T}(X|Class(all))/\sqrt{H(X)}$ for TS-X data.

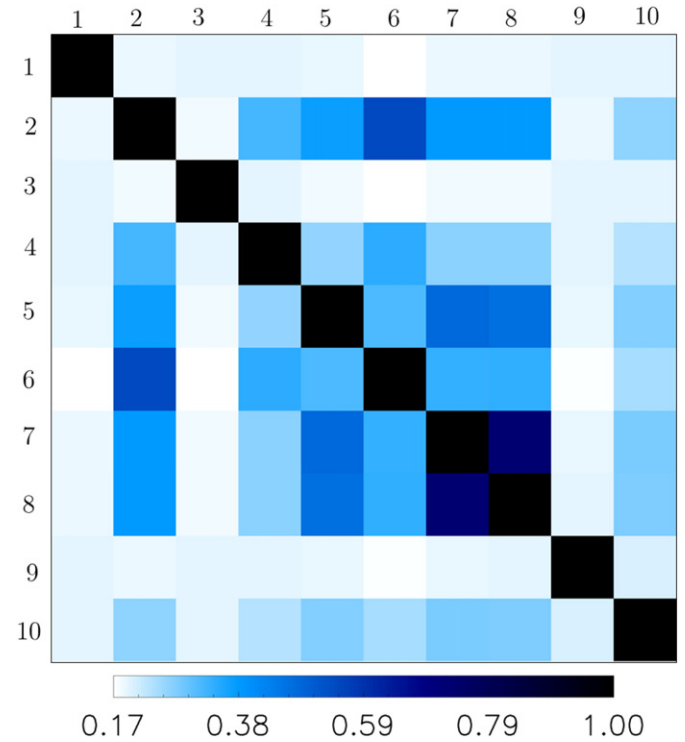| Feature	$\mathscr{T}_{(RS)}$	Feature	$\mathscr{T}_{(TSX)}$
span	0.34462485	δ	0.50492575
Rco	0.33856680	H	0.46412914
H	0.33295479	τ	0.44965620
δ	0.32991932	Rco	0.44096278
τ	0.32004349	span	0.43324989
μ	0.28796856	ρ_{CO}	0.42914710
α	0.26523526	α	0.42182257
A	0.094870827	μ	0.37953386
$\sigma_{\varphi_{co}}$	0.025278190	$\sigma_{\varphi_{co}}$	0.084320886
ρ_{CO}	0.011422892	A	0.076652909

Fig. 15. Normalized mutual information (RS-2) $\mathscr{T}(Y_1, Y_2)/\sqrt{\mathscr{H}(Y_1).\mathscr{H}(Y_2)}$. Features are: 1: $\sigma_{\varphi_{co}}$, 2: Rco, 3: ρ_{CO}, 4: μ, 5: τ, 6: span, 7: δ, 8: H, 9: A, 10: α.

methodology is tuned for operational Near Real Time Services with average processing time of 10–12 min for a standard TS-X Quad-Pol
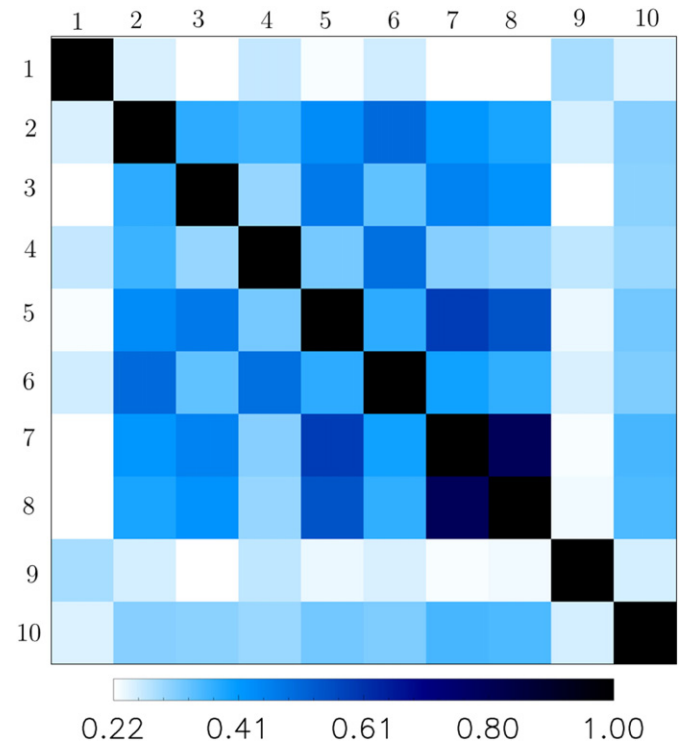

Fig. 16. Normalized mutual information (TS-X) $\mathscr{T}(Y_1, Y_2)/\sqrt{\mathscr{H}(Y_1).\mathscr{H}(Y_2)}$. Features are: 1: $\sigma_{\varphi_{co}}$, 2: Rco, 3: ρ_{CO}, 4: μ, 5: τ, 6: span, 7: δ, 8: H, 9: A, 10: α.

StripMAP scene and 7–8 min for RS-2 Fine Quad-Pol scene. An extensive evaluation of features and performance estimation of the classifier for L-band polarimetric SAR images in different environmental conditions along with exploitation of compact polarimetric features is foreseen in the near future.

References

Breit, H., Fritz, T., Balss, U., Lachaise, M., Niedermeier, A., Vonavka, M., 2010. Terrasar-x sar processing and products. Geosci. Remote Sens. IEEE Trans. 48, 727–740. http://dx.doi.org/10.1109/TGRS.2009.2035497.

Brekke, C., Solberg, A.H.S., 2005. Oil spill detection by satellite remote sensing. Remote Sens. Environ. 95, 1–13. http://dx.doi.org/10.1016/j.rse.2004.11.015 (URL: http://www.sciencedirect.com/science/article/pii/S0034425704003724).

Carpenter, A., 2016. Oil Pollution in the North Sea. 41. 1 ed. Springer International Publishing.

Cloude, S.R., Pottier, E., 1996. A review of target decomposition theorems in radar polarimetry. Geosci. Remote Sens. IEEE Trans. 34, 498–518.

Cloude, S.R., Pottier, E., 1997. An entropy based classification scheme for land applications of polarimetric SAR. Geosci. Remote Sens. IEEE Trans. 35, 68–78.

Collins, M., Denbina, M., Minchew, B., Jones, C., Holt, B., 2015. On the use of simulated airborne compact polarimetric sar for characterizing oil water mixing of the deepwater horizon oil spill. Sel. Top. Appl. Earth Obs. Remote Sens. IEEE J. 8 (3), 1062–1077. http://dx.doi.org/10.1109/JSTARS.2015.2401041.

Eineder, M., Fritz, T., 2006. Terrasar-x ground segment experimental product description. Technical Report TX-GS-DD-3303, Issue. 1.3. German Aerospace Center (DLR) (URL: http://sss.terrasar-x.dlr.de/ pdfs/TX-GS-DD-3303.pdf).

Fingas, M., Brown, C., 2014. Review of oil spill remote sensing. Mar. Pollut. Bull. 83, 9–23. http://dx.doi.org/10.1016/j.marpolbul.2014.03.059 (URL: http://www.sciencedirect.com/science/article/pii/S0025326X14002021).

Gade, M., Alpers, W., Hühnerfuss, H., Masuko, H., Kobayashi, T., 1998. Imaging of biogenic and anthropogenic ocean surface films by the multifrequency/multipolarization SIR-C/X-SAR. J. Geophys. Res. Oceans 103, 18851–18866.

Hajnsek, I., Pottier, E., Cloude, S.R., 2003. Inversion of surface parameters from polarimetric SAR. Geosci. Remote Sens. IEEE Trans. 41, 727–744.

Lange, O.F., Grubmüller, H., 2006. Generalized correlation for biomolecular dynamics. Proteins Struct. Funct. Bioinf. 62, 1053–1061. http://dx.doi.org/10.1002/prot.20784 (URL:).

Latini, D., Fratem, F.D., Jones, C.E., 2016. Multi-frequency and polarimetric quantitative analysis of the gulf of Mexico oil spill event comparing different sar systems. Remote Sens. Environ. 183, 26–42. http://dx.doi.org/10.1016/j.rse.2016.05.014 (URL: http://www.sciencedirect.com/science/article/pii/S0034425716302152).

Liu, P., Li, X., Qu, J.J., Wang, W., Zhao, C., Pichel, W., 2011. Oil spill detection with fully polarimetric UAVSAR data. Mar. Pollut. Bull. 62, 2611–2618.

Migliaccio, M., Gambardella, A., Tranfaglia, M., 2007. SAR polarimetry to observe oil spills. Geosci. Remote Sens. IEEE Trans. 45, 506–511.

Migliaccio, M., Gambardella, A., Nunziata, F., Shimada, M., Isoguchi, O., 2009a. The PALSAR polarimetric mode for sea oil slick observation. IEEE Trans. Geosci. Remote Sens. 47, 4032–4041. http://dx.doi.org/10.1109/TGRS.2009.2028737.

Migliaccio, M., Nunziata, F., Gambardella, A., 2009b. On the co-polarized phase difference for oil spill observation. Int. J. Remote Sens. 30, 1587–1602. http://dx.doi.org/10.1080/01431160802520741.

Minchew, B., 2012. Determining the mixing of oil and sea water using polarimetric synthetic aperture radar. Geophys. Res. Lett. 39, 1–6. http://dx.doi.org/10.1029/2012GL052304 (URL:, 116607).

Mittermayer, J., Runge, H., 2003. Conceptual studies for exploiting the terrasar-x dual receive antenna. Geoscience and Remote Sensing Symposium, 2003. IGARSS '03. Proceedings. 2003 IEEE International, pp. 2140–2142 http://dx.doi.org/10.1109/IGARSS.2003.1294365.

Nissen, S., 2005. Neural Networks Made Simple. Technical Report 2.

Nunziata, F., Gambardella, A., Migliaccio, M., 2008. On the Mueller scattering matrix for SAR sea oil slick observation. Geosci. Remote Sens. Lett. IEEE 5, 691–695.

Nunziata, F., Migliaccio, M., Gambardella, A., 2011. Pedestal height for sea oil slick observation. IET Radar Sonar Navig. 5 (7), 103–110.

Peng, H., Long, F., Ding, C., 2005. Feature selection based on mutual information criteria of max-dependency, max-relevance, and min-redundancy. Pattern Anal. Mach. Intell. IEEE Trans. 27, 1226–1238. http://dx.doi.org/10.1109/TPAMI.2005.159.

Praks, J., Koeniguer, E., Hallikainen, M., 2009. Alternatives to target entropy and alpha angle in SAR polarimetry. Geosci. Remote Sens. IEEE Trans. 47, 2262–2274. http://dx.doi.org/10.1109/TGRS.2009.2013459.

Ressel, R., Singha, S., 2016. Comparing near coincident space borne C and X band fully polarimetric sar data for arctic sea ice classification. Remote Sens. 8, 198. http://dx.doi.org/10.3390/rs8030198 (URL: http://www.mdpi.com/2072-4292/8/3/198).

Ressel, R., Frost, A., Lehner, S., 2015. Investigating the potential of different polarimetric features based on dual polarimetric TerraSAR-X data for automated sea ice classification. Proceedings of the POLINSAR 2015, p. SP-729.

Singha, S., Vespe, M., Trieschmann, O., 2013. Automatic synthetic aperture radar based oil spill detection and performance estimation via a semi-automatic operational service benchmark. Mar. Pollut. Bull. 73, 199–209. http://dx.doi.org/10.1016/j.marpolbul.2013.05.022 (pmid:23790462).

Singha, S., Velotto, D., Lehner, S., 2014. Near real time monitoring of platform sourced pollution using TerraSAR-X over the North Sea. Mar. Pollut. Bull. 86, 379–390.

Singha, S., Ressel, R., Velotto, D., Lehner, S., 2016. A combination of traditional and polarimetric features for oil spill detection using terrasar-x. IEEE J. Sel. Top. Appl. Earth Obs. Remote Sens. 1–12.

Skrunes, S., Brekke, C., Eltoft, T., 2014a. Characterization of marine surface slicks by Radarsat-2 multipolarization features. Geosci. Remote Sens. IEEE Trans. 52, 5302–5319.

Skrunes, S., Brekke, C., Eltoft, T., Kudryavtsev, V., 2014b. Comparing near-coincident C-and X-Band SAR acquisitions of marine oil spills. Geosci. Remote Sens. IEEE Trans. 53, 1958–1975.

Solberg, A.H.S., 2012. Remote sensing of ocean oil-spill pollution. Proc. IEEE 100, 2931–2945.

Strehl, A., Ghosh, J., 2003. Cluster ensembles — a knowledge reuse framework for combining multiple partitions. J. Mach. Learn. Res. 3, 583–617. http://dx.doi.org/10.1162/153244303321897735 (URL:).

Topouzelis, K.N., 2008. Oil spill detection by SAR images: dark formation detection, feature extraction and classification algorithms. Sensors 8, 6642–6659.

Velotto, D., Nunziata, F., Migliaccio, M., Lehner, S., 2011. Dual-polarized TerraSAR-X data for oil-spill observation. Geosci. Remote Sens. IEEE Trans. 49, 1114–1118.

Yu, L., Liu, H., 2003. Feature selection for high-dimensional data: a fast correlation-based filter solution. Proceedings of the 20th International Conference on Machine Learning (ICML-03), pp. 856–863.

Zhang, B., Perrie, W., Li, X., Pichel, W.G., 2011. Mapping sea surface oil slicks using radarsat-2 quad-polarization sar image. Geophys. Res. Lett. 38, L10602. http://dx.doi.org/10.1029/2011GL047013 (n/a–n/a. URL:).